Enhanced flux of extraterrestrial ^{3}He across the Permian–Triassic boundary

Tetsuji Onoue[1*], Naoto Takahata[2], Mitsutaka Miura[1], Honami Sato[3], Akira Ishikawa[4], Katsuhito Soda[1], Yuji Sano[2] and Yukio Isozaki[5]

Abstract

The *ca* 252 Ma Permian–Triassic boundary (PTB) represents the most severe mass extinction event of the Phanerozoic, with the disappearance of ~ 80% of marine invertebrate species. Large-scale eruption of the Siberian Traps is the commonly favored cause, although the link between volcanism and extinction remains debated. Here, we report evidence for an extraterrestrial ^{3}He influx in the PTB section of deep-sea bedded cherts from Japan. This unusual signal indicates a significant increase in the influx of interplanetary dust particles, likely related to an asteroid shower in the inner solar system. High-resolution stratigraphy indicates that the peak flux of dust particles occurred during the final 500 kyr of the Permian, concurrent with a pre-extinction decline in radiolarian diversity.

Keywords: Permian, Triassic, Bedded chert, Mino Belt, Helium, Platinum group element, Interplanetary dust particle, Radiolaria

Introduction

The Permian–Triassic boundary (PTB) mass extinction event (MEE) (Erwin 1994; Wignall 2007) was associated with catastrophic environmental changes including oceanic anoxia, global carbon cycle perturbations, methane hydrate release, and global warming (Isozaki 1997; Wignall 2007; Burgess et al. 2014). The release of volcanic and contact metamorphic carbon and sulfur gases (CO_2, CH_4, and SO_2) from the Siberian Traps is commonly invoked as the trigger for climatic perturbations across the PTB (Wignall 2007; Burgess et al. 2017), which led to the end-Permian MEE. Although extraterrestrial causes have been proposed (e.g., bolide impact, Becker et al. 2001, 2004; Basu et al. 2003), they have not been favored (Koeberl et al. 2004; Farley et al. 2005), largely due to a lack of geochemical and mineralogical evidence such as platinum group element (PGE) anomalies and shocked quartz. The accretion of extraterrestrial noble gases such as He and Ar was discussed by Becker et al. (2001), who reported high concentrations of extraterrestrial He (^{3}He$_{ET}$) in PTB rocks from Japan and China, with a suggestion that ^{3}He$_{ET}$ is trapped in

fullerenes associated with an impact event (Becker et al. 2001). However, the reported ^{3}He$_{ET}$ and fullerene concentrations have not been reproduced in independent analyses of the same samples and others from PTB sections in China, Canada, and Austria (Koeberl et al. 2004; Farley et al. 2005).

The solar system contains abundant sub-millimeter interplanetary dust particles (IDPs) enriched in ^{3}He, and ^{3}He concentrations in ancient deep-sea sediments have been used to constrain the IDP flux to Earth over at least the last 100 Myr (Farley 1995; Farley et al. 2012). However, the use of ^{3}He in detecting IDPs is often compromised by the diffusional loss of ^{3}He from sedimentary rocks (Farley et al. 2005; Mukhopadhyay and Farley 2006), with the exception of some Ordovician samples that record a period of unusually high extraterrestrial ^{3}He flux (Patterson et al. 1998).

This is the first report of preservation of ^{3}He$_{ET}$ in Permian bedded chert and overlying Triassic black claystone from Waidani (Sano et al. 2010, 2012a), Japan, which was deposited in the Panthalassa superocean (Isozaki 1997) and subsequently accreted to the Japan margin during the Jurassic. Biostratigraphic and chemostratigraphic data indicate that this PTB section preserves a complete pelagic PTB transition, without a temporal gap at lithological contacts between bedded chert and

* Correspondence: t_onoue@kumamoto-u.ac.jp
[1]Department of Earth and Environmental Sciences, Kumamoto University, Kumamoto 860-8555, Japan
Full list of author information is available at the end of the article

black claystone (Sano et al. 2010, 2012a; Agematsu et al. 2014). The $^3He_{ET}$ flux across the PTB was calculated on the basis of $^3He_{ET}$ concentrations and sedimentary mass accumulation rates estimated from the astronomically tuned cyclostratigraphy of the bedded chert. The $^3He_{ET}$ record is supported by PGE concentrations measured in bulk rock samples from the section, and their major and trace element compositions.
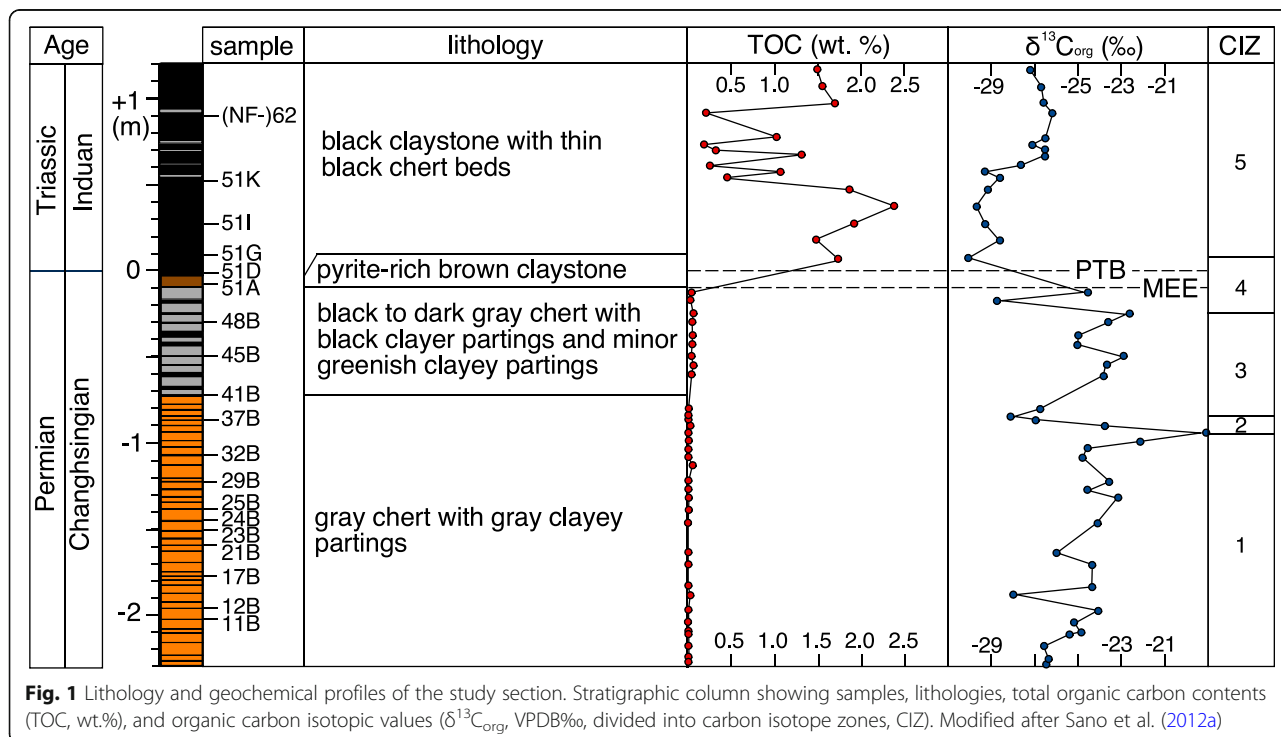
Methods/Experimental
Sample collection and preparation
Samples for whole-rock He isotopic analyses were collected from the siliceous PTB section of the Mino Belt, Japan, which is a Jurassic subduction-generated accretionary complex (Additional file 1: Figure S1). PTB siliceous rocks of the Mino Belt are considered to be long-lived Panthalassa remnants representing an allochthonous proto-Pacific Plate assemblage (Matsuda and Isozaki 1991; Isozaki 1997). The bedded cherts lack carbonate and coarse terrigenous grains, suggesting that their primary depositional site was deeper than the calcium carbonate compensation depth and beyond the depositional range of terrigenous clastic grains (Matsuda and Isozaki 1991; Isozaki 1997). PTB siliceous rocks in Japan are characterized by a very low sedimentation rate (less than a few millimeters per kyr), an absence of coarse-grained terrigenous clastics, and fine-grained sediment compositions (mainly cryptocrystalline quartz). They contain small extraterrestrial particles, including well-preserved melted and

unmelted micrometeorites, and cosmic spinels (Onoue et al. 2011, 2012; Uno et al. 2012).

The studied section crops out along a road cutting near Waidani in the Mt. Funabuseyama area of the Mino Belt, central Japan (Additional file 2: Figure S2). The examined rocks correspond to the Permian–Lower Triassic Hashikadani Formation, which is characterized by pelagic, deep-sea siliceous sediments (Sano et al. 2012a). The section was referred to as NF1212R and NF1212C in previous studies (Sano et al. 2010, 2012), but the term "Waidani section" is used here.

The Waidani section comprises a 3.5 m thick continuous succession of gray and dark gray bedded chert overlain by black claystone, with a pyrite-rich brown claystone layer at its base (Fig. 1). The bedded chert comprises rhythmically alternating beds of chert and relatively thin beds of claystone. Based on high-resolution radiolarian and conodont biostratigraphy (Sano et al. 2010; Agematsu et al. 2014), the bedded chert in the section is assigned to the Upper Permian (Changhsingian), and the overlying black claystone to the lowermost Triassic (Griesbachian). A negative excursion in organic carbon isotopic ratios ($\delta^{13}C_{org}$) occurs at the top of the dark gray bedded chert (Sano et al. 2012a), coinciding with radiolarian fossil disappearances correlated with the MEE horizon in other PTB sections (Feng and Algeo 2014). The Triassic base of the section is defined by the presence of natural assemblages of the conodont *Hindeodus* (*H. parvus* and *H. typicalis*) in the

Fig. 1 Lithology and geochemical profiles of the study section. Stratigraphic column showing samples, lithologies, total organic carbon contents (TOC, wt.%), and organic carbon isotopic values ($\delta^{13}C_{org}$, VPDB‰, divided into carbon isotope zones, CIZ). Modified after Sano et al. (2012a)

basal 15 cm thick stratigraphic interval of black clays-tone (Agematsu et al. 2014).

To avoid variations in chemistry related to lithological changes (Farley et al. 2005), all samples for whole-rock geochemical analysis were collected from claystone beds: 13 Permian claystones and 1 brown and 5 dark gray Triassic claystones. Veins and strongly recrystallized and/or weathered parts of the claystone beds were avoided to minimize effects of diagenetic overprinting on sediment geochemistry. Samples contain brown conodont elements (Agematsu et al. 2014), with a conodont color alteration index (CAI) of 2, indicating that the rocks were exposed to burial temperatures of 60–140 °C.

He isotopic analysis

Prior to He isotopic analysis, the samples were crushed and washed with ultrapure water; after drying, the fragments were carefully hand-picked to avoid contamination by altered and weathered material, and hand-picked fragments (< 5 mm grain size, 10–20 g) were pulverized in an agate mortar.

Both bulk and stepped heating methods were used to determine He concentrations and ^{3}He/^{4}He ratios. The bulk method was applied to 19 samples and involved gas extraction by melting samples at 1800 °C. The stepped heating method (Amari and Ozima 1985; Farley et al. 2005; Mukhopadhyay and Farley 2006) was used to identify the ^{3}He carrier in the most ^{3}He-rich sample (NF-37B): heating began at 550 °C increasing in 100 °C steps, with 30–50 min per step.

Cleaned and homogenized powder samples (0.25 g for the bulk method, ~ 1 g for the stepped method) were wrapped in Al foil and placed in the loading port. Samples were preheated under vacuum at 110 °C for 11 h to drive off adsorbed gases. Samples were then fused under vacuum at a maximum temperature of 1800 °C to extract trapped gases, which were purified using a charcoal trap at liquid nitrogen temperature and with a hot titanium getter. After purification, ^{4}He and ^{20}Ne abundances and ^{4}He/^{20}Ne ratios were determined using a quadrupole mass spectrometer, and He concentrations and ^{3}He/^{4}He ratios using a noble gas mass spectrometer (Helix-SFT; GV Instruments) at the Atmosphere and Ocean Research Institute, University of Tokyo, Tokyo, Japan. Meteorite samples had not previously been analyzed by this measurement system. Air was used as a standard for noble gas isotopic analyses (Sano et al. 2013). He blanks (3 × 10^{-15} cm^3 STP for ^{3}He; 3 × 10^{-9} cm^3 STP for ^{4}He) were < 20% of the sample signal.

Acid leaching procedure

Most IDPs found on Earth's surface comprise aggregates of small grains of olivine, pyroxene, Fe–Ni sulfides, and magnetite (Genge et al. 2008). Previous investigations of

a Triassic bedded chert unit from the study area identified IDPs preserved with silicate phases (olivine and pyroxene, Onoue et al. 2011). If these minerals act as carrier phases for extraterrestrial ^{3}He, most ^{3}He would be lost during acid leaching (Mukhopadhyay and Farley 2006). Four bulk samples were selected that yielded high (NF-37B, 41B) and low (NF-25B, 51I) ^{3}He concentrations. The samples were treated with a 12M HF–3M HCl mixture for 48 h at room temperature, rinsed four times with ultrapure water, and dried. He was extracted at temperatures of 750 °C, 950 °C, and 1800 °C during heating in a furnace.

Estimation of extraterrestrial ^{3}He concentrations

^{3}He$_{ET}$ concentrations in sediments were calculated using the following equation (Marcantonio et al. 1995):

$$\left[^3\text{He}_{ET}\right] = \left(1 - R_{\text{terrigenous}}/R_{\text{measured}}\right)/\left(1 - R_{\text{terrigenous}}/R_{\text{IDP}}\right) \\ \times \left[^3\text{He}_{\text{measured}}\right]$$

(1)

where $R_{\text{terrigenous}}$ and R_{IDP} are ^{3}He/^{4}He ratios for terrigenous (^{3}He/^{4}He = 0.015 Ra, Sano 2017) and extraterrestrial (^{3}He/^{4}He = 170 Ra, McGee and Mukhopadhyay 2013) end-members, respectively (Ra = atmospheric ^{3}He/^{4}He ratio = 1.382 × 10^{-6}, Sano 2017). The lack of volcanic material in the analyzed samples precludes the presence of trapped mantle He. The lowest ^{3}He/^{4}He ratio (0.2 Ra) was measured in Triassic beds, with the fraction of extraterrestrial ^{3}He exceeding 90%.

Platinum group element analysis

Platinum group elements (Ir, Ru, Pt, and Pd) and Re were analyzed by isotope dilution mass spectrometry (ID–MS) after quartz tube digestion. Sample digestion, purification, and mass spectrometry were based on procedures described by Ishikawa et al. (2014). Powdered samples (~ 0.1 g) and spike solutions containing ^{185}Re and ^{191}Ir–^{99}Ru–^{196}Pt–^{105}Pd were transferred to a quartz tube. After the addition of 2 mL of inverse *aqua regia*, the tubes were frozen in dry ice–ethanol, sealed with an oxypropane torch, and placed in an oven at 240 °C for 72 h. HF (1 mL, 38%) was added to the residue for desilicification (Ishikawa et al. 2014).

Platinum group element isotopic compositions of purified sample solutions were determined by inductively coupled plasma mass spectrometry (ICP–MS, Thermo-Element XR) at the University of Tokyo, Komaba, Japan. Sample and standard solutions were interspersed throughout analytical sessions to monitor and correct for instrumental fractionation; ^{89}Y, ^{90}Zr, ^{95}Mo, ^{97}Mo, ^{99}Ru, ^{100}Ru, ^{101}Ru, ^{105}Pd, ^{106}Pd, ^{108}Pd, ^{111}Cd ^{178}Hf, ^{185}Re, ^{187}Re, ^{191}Ir, ^{193}Ir, ^{194}Pt, ^{195}Pt, ^{196}Pt, and ^{202}Hg were monitored for possible mass interference. Raw

signal intensities were corrected using measured isobaric–oxide interferences, although contributions of interferences to sample signals were insignificant (< 0.1%).

Elemental concentrations were corrected using average total procedural blanks obtained from each batch of analyses (0.7 pg Ir, 2.3 pg Ru, 13 pg Pt, 10 pg Pd, and 0.3 pg Re; $n = 2$). Uncertainties for each sample were estimated by error propagation through ICP–MS measurements (2SE) and blank corrections (< 51%). Blank contributions of Ir, Pt, Pd, and Re were < 12%, < 6%, < 9%, and < 7%, respectively, while the contribution to Ru was slightly higher (5–26%, < 41% for sample NF-21B).

Major and trace element analyses
Major element contents of 21 samples were determined by X-ray fluorescence spectrometry (XRF, PANalytical Epsilon 3XLE with a Mo X-ray tube) on pressed powder pellets, at Kumamoto University, Kumamoto, Japan. Standard rock samples issued by the Geological Survey of Japan were used for calibration purposes. Reproducibility, based on four repeat analyses of standard JSd-1, was better than ± 0.5% for Mg, Al, Si, K, Ca, Ti, and Fe and better than ± 1% for Na and Mn.

Nineteen samples were analyzed for trace and rare earth elements (REE) by ICP–MS after lithium metaborate/tetraborate fusion at Actlabs, Ancaster, Canada. Ten international rock and mineral standards were analyzed for quality control purposes during trace element and REE analyses. Analytical procedures are described in http://www.actlabs.com.

Estimation of sedimentation rate for Changhsingian bedded chert
The average sedimentation rate for Changhsingian bedded chert of the Hashikadani Formation was estimated for a PTB section at Iwaidani (NF195 section; Sano et al. 2012b), cropping out ~ 3 km from the Waidani section (Additional file 2: Figure S2). Lithologically, the NF195 section is very similar to the Waidani section (Sano et al. 2010, 2012b), comprising a lower unit (~ 6.2 m thick) of gray bedded chert, a middle unit (~ 0.7 m thick) of black bedded chert including pyrite nodules near the top, and an upper unit (~ 0.9 m thick) characterized by black claystone with thin black chert beds. Biostratigraphic analysis of radiolarians reveals that the section contains the Wuchiapingian–Changhsingian boundary in the basal ~ 0.3 m of the lower unit and an MEE horizon at the top of the middle unit. The stratigraphic range of the Changhsingian is ~ 6.6 m, and its duration was 2.20 ± 0.16 Myr according to U–Pb ages for the MEE (251.941 ± 0.037 Ma, Burgess et al. 2014) and Wuchiapingian–Changhsingian boundary (254.14 ± 0.12 Ma, Ramezani and Bowring 2017). From these data, the average sedimentation rate for the Changhsingian

bedded chert of the Hashikadani Formation is estimated to be ~ 0.3 cm kyr^{-1}.

Time-series analysis
The bedded chert in the studied section comprises rhythmically alternating beds of chert (1–7 cm thick) and relatively thin beds of claystone (1–2 cm thick). Individual chert and claystone thicknesses were measured throughout the section, with "silica ranks" of 0 for claystone and 1 for chert being assigned. Cyclostratigraphic analyses of the Triassic–Jurassic bedded chert sequence were based on bed thicknesses in the Mino Belt (Ikeda and Tada 2014). However, Algeo et al. (2011) suggest that other methods should be used where analyzed intervals are too short for estimating sedimentation rates or to capture astronomical cycles such as the 405 kyr eccentricity cycles (Laskar et al. 2004). Sedimentation rates for the Upper Permian bedded chert sequence were therefore estimated using orbital tuning procedures involving long precession cycles (Yao et al. 2015). Periodicities and modulations in time–frequency space were estimated using REDFIT software (Schulz and Mudelsee 2002) and continuous wavelet analyses with Morlet mother signals (Torrence and Compo 1998). Bandpass filters with Gaussian windows (Paillard et al. 1996) were applied to extract astronomical signals from binary series.

Results
He analyses
Analyzed samples yielded bulk ^{3}He and ^{4}He concentrations of 0.05–0.34 × 10^{-12} cm^3 STP g^{-1} and 0.09–0.47 × 10^{-6} cm^3 STP g^{-1}, respectively (Table 1). ^{3}He concentrations are highest in the topmost ~ 1.5 m of the studied Permian deposits (Fig. 2a), with a maximum ^{3}He concentration of 0.34 × 10^{-12} cm^3 STP g^{-1}, which is 4–5 times greater than that measured in the overlying Triassic unit.

The analyzed samples likely preserve primary fluctuations in ^{3}He concentrations across the PTB because (1) the detected ^{4}He/^{20}Ne ratios are > 100 times greater than the atmospheric value, thereby precluding the existence of significant atmospheric He in the samples and (2) the lack of correlation ($r^2 = 0.3$) between ^{3}He and ^{4}He concentrations suggests that the increase in ^{3}He during the uppermost Permian cannot be explained by He retention alone. ^{3}He/^{4}He ratios follow a similar trend to ^{3}He concentrations, with the maximum ^{3}He/^{4}He ratio of 0.75 Ra being measured in the uppermost Permian bed.

Stepped heating
To identify the source of the high ^{3}He/^{4}He signature, stepwise heating of the sample with the highest ^{3}He concentration (NF-37B) was performed at 550 °C, 650 °C, 750 °C,

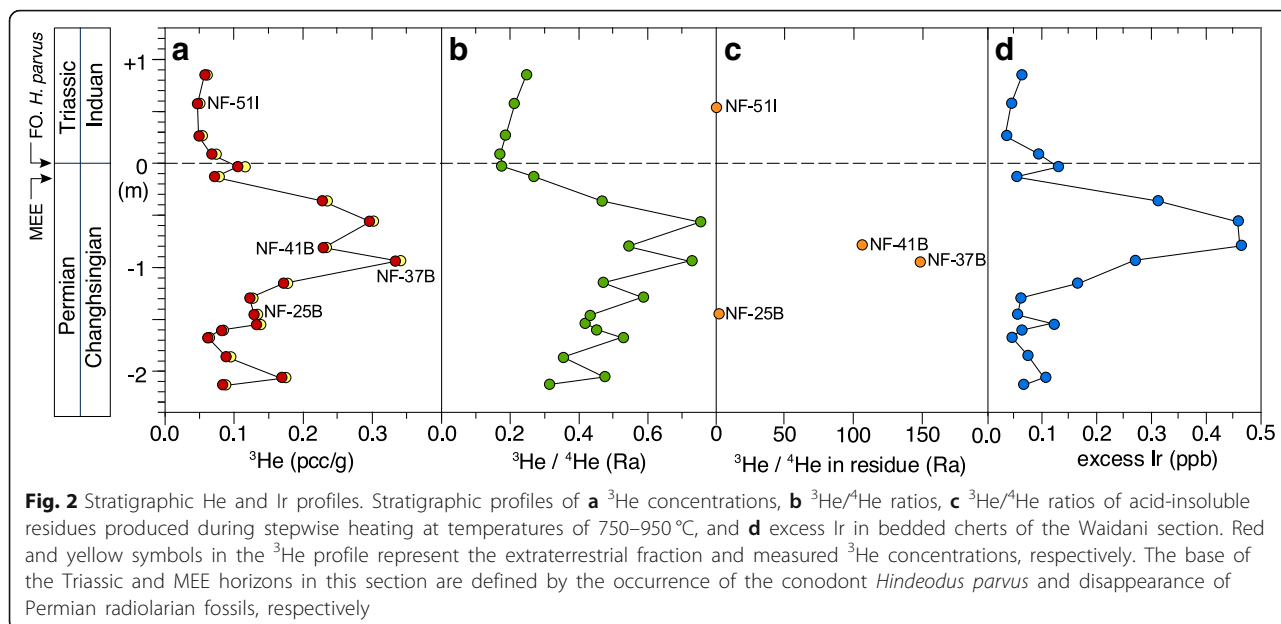**Table 1** ^{3}He and ^{4}He concentrations, and ^{3}He/^{4}He ratios for samples from the Waidani section

Sample	Height (m)	MAR* (g cm^{-2} kyr^{-1})	Temperature (°C)	^{3}He (pcc g^{-1})	^{4}He (µcc g^{-1})	^{3}He /^{4}He (R_a)#	min ^{4}He/^{20}Ne	^{3}He$_{ET}$ (pcc g^{-1})	^{3}He$_{ET}$ flux (pcc cm^{-2} kyr^{-1})
				Bulk					
NF-62	0.88		1800	0.06	0.18	0.25 ± 0.04	40	0.06	
NF-51 K	0.60		1800	0.05	0.17	0.22 ± 0.03	26	0.05	
NF-51I	0.30		1800	0.05	0.20	0.19 ± 0.03	53	0.05	
NF-51G	0.12		1800	0.08	0.32	0.17 ± 0.03	70	0.07	
NF-51D	0.00		1800	0.12	0.47	0.18 ± 0.02	49	0.11	
NF-51A	−0.10		1800	0.08	0.21	0.27 ± 0.03	44	0.08	
NF-48B	−0.33	0.81 ± 0.18	1800	0.23	0.36	0.47 ± 0.02	37	0.23	0.18 ± 0.05
NF-45B	−0.53	0.81 ± 0.18	1800	0.30	0.29	0.75 ± 0.02	82	0.30	0.24 ± 0.05
NF-41B	−0.76	0.81 ± 0.18	1800	0.24	0.32	0.55 ± 0.02	211	0.23	0.19 ± 0.04
NF-37B	−0.90	0.81 ± 0.18	1800	0.34	0.34	0.72 ± 0.02	37	0.34	0.27 ± 0.06
NF-32B	−1.11	0.81 ± 0.18	1800	0.18	0.27	0.47 ± 0.02	49	0.17	0.14 ± 0.03
NF-29B	−1.25	0.81 ± 0.18	1800	0.13	0.15	0.59 ± 0.02	37	0.12	0.10 ± 0.02
NF-25B	−1.42	0.81 ± 0.18	1800	0.13	0.22	0.43 ± 0.02	58	0.13	0.10 ± 0.02
NF-24B	−1.50	0.81 ± 0.18	1800	0.14	0.24	0.42 ± 0.02	60	0.13	0.11 ± 0.02
NF-23B	−1.56	0.81 ± 0.18	1800	0.09	0.14	0.45 ± 0.03	36	0.08	0.07 ± 0.02
NF-21B	−1.63	0.81 ± 0.18	1800	0.07	0.09	0.53 ± 0.03	22	0.06	0.05 ± 0.01
NF-17B	−1.82	0.81 ± 0.18	1800	0.10	0.19	0.35 ± 0.03	34	0.09	0.07 ± 0.02
NF-12B	−2.01	0.81 ± 0.18	1800	0.18	0.27	0.48 ± 0.02	38	0.17	0.14 ± 0.03
NF-11B	−2.08	0.81 ± 0.18	1800	0.09	0.21	0.32 ± 0.03	13	0.09	0.07 ± 0.02
blank				0.01	0.01				
air						1.00	0.32		
				Stepwise heating					
NF-37B	−0.90		550	0.075	0.232	0.23 ± 0.02	194		
NF-37B	−0.90		650	0.071	0.054	0.95 ± 0.02	48		
NF-37B	−0.90		750	0.067	0.009	5.22 ± 0.09	13		
NF-37B	−0.90		850	0.071	0.004	13.5 ± 0.2	6		
NF-37B	−0.90		950	0.019	0.001	13.9 ± 0.5	5		
NF-37B	−0.90		1800	0.006	0.001	3.80 ± 0.22	2		
NF-37B	−0.90		total	0.31	0.30	0.73			
				12 M HF–3 M HCl dissolution					
NF-51I	0.60		750–950	0.002	0.001	1.22 ± 0.07	143		
NF-41B	−0.76		750–950	0.014	< 0.001	107.1 ± 1.9	33		
NF-37B	−0.90		750–950	0.007	< 0.001	149.7 ± 8.8	10		
NF-37B	−0.90		950–1800	0.003	< 0.001	16.6 ± 0.7	34		
NF-25B	−1.42		750–950	< 0.001	< 0.001	2.98 ± 0.27	45		

*Based on the sedimentation rate (mean ± 2SD) derived from an astronomically tuned cyclostratigraphy age model for the Permian section
#Error assigned to the isotopic ratio is 1σ

850 °C, 950 °C, and 1800 °C (Fig. 3), resulting in extraction of He from different mineral phases, which was analyzed for ^{3}He/^{4}He ratios at each step. Most ^{4}He was extracted at the lowest step (550 °C), while ~ 50% of ^{3}He was released at intermediate temperatures (750 °C and 850 °C). This decoupled behavior indicates that ^{3}He and ^{4}He are hosted in separate phases within the sample. Previous studies indicate that ^{3}He hosted in IDPs is released at temperatures

Fig. 2 Stratigraphic He and Ir profiles. Stratigraphic profiles of **a** ^{3}He concentrations, **b** ^{3}He/^{4}He ratios, **c** ^{3}He/^{4}He ratios of acid-insoluble residues produced during stepwise heating at temperatures of 750–950 °C, and **d** excess Ir in bedded cherts of the Waidani section. Red and yellow symbols in the ^{3}He profile represent the extraterrestrial fraction and measured ^{3}He concentrations, respectively. The base of the Triassic and MEE horizons in this section are defined by the occurrence of the conodont *Hindeodus parvus* and disappearance of Permian radiolarian fossils, respectively

of > 800 °C (Farley et al. 2005). Helium extracted at 850 °C from sample NF-37B is similar to that in IDPs in terms of ^{3}He release temperature and high ^{3}He/^{4}He ratios (14 Ra), whereas the component released at 550 °C has a much lower ^{3}He/^{4}He ratio (0.2 Ra). The temperature range over

Fig. 3 Results of the stepwise heating experiments. ^{3}He (**a**) and ^{4}He (**b**) release profiles as a function of temperature for sample NF-37B. ^{3}He/^{4}He ratios for NF-37B are shown in each panel for comparison. Helium extracted at 850 °C yielded a high ^{3}He/^{4}He ratio (14 Ra), suggesting release from IDPs. The stratigraphic level of sample NF-37B is shown in Fig. 2

which ^{3}He was released (550–850 °C) is equivalent to that determined for the decomposition of IDPs (Farley et al. 2005). Our results therefore indicate that the unusually high ^{3}He concentration in the studied PTB section is of extraterrestrial origin and is likely hosted in IDPs.
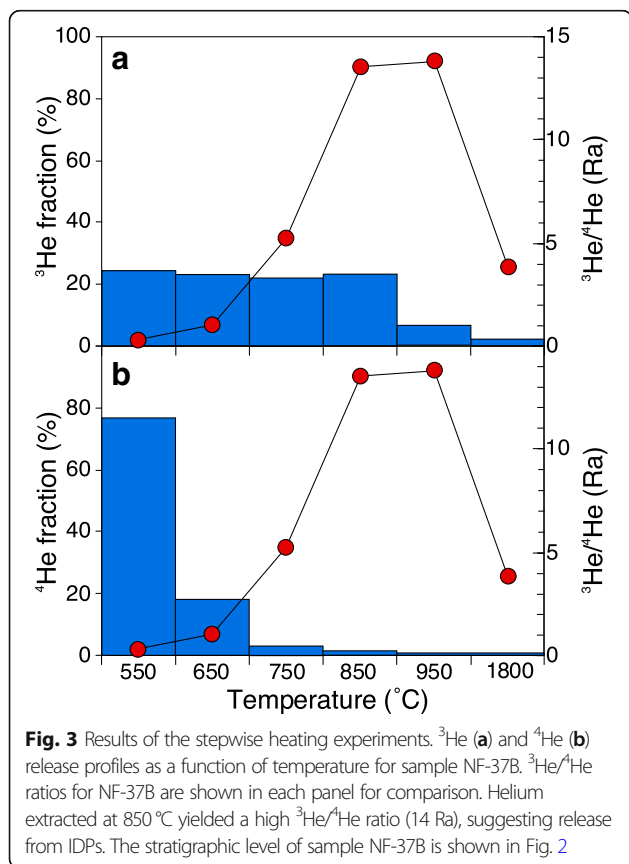
An acid leaching procedure (Mukhopadhyay and Farley 2006) was applied to the PTB samples to confirm the existence of extraterrestrial He. High ^{3}He/^{4}He ratios (up to 150 Ra) were detected during the extraction of He at 750–950 °C from acid-insoluble residues produced from samples with high ^{3}He concentrations (NF-37B, 41B). Low-^{3}He samples (NF-25B, 51I) have low ^{3}He/^{4}He ratios (< 3 Ra, Fig. 2c), with > 96% of ^{3}He being removed during leaching. We therefore interpret the high ^{3}He/^{4}He ratios as recording the existence of extraterrestrial He, hosted mainly in IDPs.

HF–HCl-resistant refractory phases found in meteorites include spinel, corundum, diamond, graphite, SiC, amorphous carbon, and organic material (Patterson et al. 1998). Previous studies excluded such phases (except for spinel) as possible long-term carriers of ^{3}He$_{ET}$ (Mukhopadhyay and Farley 2006). A Middle Ordovician (~ 470 Ma) shallow marine limestone in Sweden, which records clear evidence of an asteroid breakup or meteorite shower event, contains ^{3}He$_{ET}$ hosted primarily in chromite (Heck et al. 2008). For our samples, we consider that extraterrestrial spinel and/or relict silicate grains may host ^{3}He in acid-insoluble residues.

Stratigraphic distribution of extraterrestrial material
The extraterrestrial fraction of ^{3}He across the PTB (Eq. (1)) indicates that bulk ^{3}He concentrations in the PTB section are highly sensitive to extraterrestrial input.

Furthermore, $^3\text{He}_{\text{ET}}$ concentrations in the topmost ~ 1.5 m of the uppermost Permian section are at least four times higher those in the pre-event interval. Platinum group elements such as Ir and Pt are often used as tracers of extraterrestrial material. As with concentrations of $^3\text{He}_{\text{ET}}$, an increase in Pt, Pd, Ru, and Ir concentrations (Table 2) occurs in the topmost ~ 1.5 m of the uppermost Permian section (Fig. 4). Iridium is the least mobile PGE (Evans et al. 1993), and excess Ir concentrations (Ir_{XS}) were calculated using the equation:

$$\text{Ir}_{\text{XS}} = \text{Ir}_{\text{measured}} - \text{Al}_{\text{measured}} \times \left(\text{Ir}_{\text{terrigenous}}/\text{Al}_{\text{terrigenous}}\right) \tag{2}$$

where "terrigenous" indicates the average value for the upper continental crust (McLennan 2001). This calculation subtracts the terrigenous Ir (supplied primarily by aeolian dust) from the total Ir content of PTB sediments, allowing the extraterrestrial contribution to be determined. The similar durations and magnitudes (4–6 times) of increases in Ir_{XS} and $^3\text{He}_{\text{ET}}$ (Fig. 2), and the good positive correlation ($r^2 = 0.7$) between them (Fig. 5), support our interpretation of enhanced extraterrestrial ^3He in the uppermost Permian and its change across the PTB. Previous studies indicate that Fe–Mn oxyhydroxides contain significant amounts of Ir, which may be remobilized when they are reduced (Colodner et al. 1992). However, reducing conditions were prominent throughout the Upper Permian (Changhsingian) (Isozaki 1997; Sano et al. 2012a; Takahashi et al. 2014) and an oxic-to-anoxic transition was not detected within the studied interval (Sano et al. 2012a) (Additional file 3: Figure S3). Indeed, there is no strong correlation between Ir and redox-sensitive elements such as Fe, Mn, V, Ni, Co, Mo, or U (Additional file 4: Figure S4).

Discussion

Our results provide no evidence of elevated $^3\text{He}_{\text{ET}}$ levels at the PTB itself, consistent with previous work on other PTB sections (Farley and Mukhopadhyay 2001; Farley et al. 2005). However, concentrations of $^3\text{He}_{\text{ET}}$ in the PTB section here indicate an abrupt and significant increase in the topmost ~ 1.5 m of the uppermost Permian section. Although He isotopic compositions may be influenced by provenance composition (Winckler and Fischer 2006), the uniform values of terrigenous elemental ratios (e.g., constant Mg/Al, Ti/Al, and Zr/Hf ratios; Additional file 5: Table S1 and Additional file 6: Table S2) indicate no effects on the stratigraphic increase of ^3He by changes of provenance composition of the Permian and Triassic deposits. The contribution of cosmogenic ^3He can also be ignored because the studied rocks were excavated some years previously from a shielded location (2–3 m underground) during road cutting.

Table 2 PGE concentrations in claystone samples from the Waidani section

| Sample	Height (m)	Ir (ppb ± 2SE)	Ru (ppb ± 2SE)	Pt (ppb ± 2SE)	Pd (ppb ± 2SE)	Re (ppb ± 2SE)
NF-62	0.88	0.085 ± 0.021	0.117 ± 0.007	2.92 ± 0.14	3.09 ± 0.17	12.5 ± 0.3
NF-51 K	0.60	0.062 ± 0.023	0.114 ± 0.009	3.97 ± 0.19	3.07 ± 0.20	44.9 ± 1.7
NF-51I	0.30	0.052 ± 0.022	0.089 ± 0.007	2.64 ± 0.12	2.05 ± 0.11	18.5 ± 0.4
NF-51G	0.12	0.114 ± 0.021	0.094 ± 0.008	3.15 ± 0.13	1.85 ± 0.35	10.7 ± 0.2
NF-51D	0.00	0.154 ± 0.022	0.151 ± 0.009	2.65 ± 0.13	1.13 ± 0.17	1.01 ± 0.02
NF-51A	− 0.10	0.076 ± 0.024	0.123 ± 0.007	3.84 ± 0.18	1.72 ± 0.43	1.42 ± 0.03
NF-48B	−0.33	0.339 ± 0.042	0.365 ± 0.009	11.3 ± 0.3	7.71 ± 0.28	0.366 ± 0.009
NF-45B	−0.53	0.479 ± 0.031	0.180 ± 0.007	14.7 ± 0.4	6.28 ± 0.25	0.079 ± 0.006
NF-41B	−0.76	0.484 ± 0.035	0.242 ± 0.007	15.4 ± 0.5	6.97 ± 0.32	0.179 ± 0.008
NF-37B	−0.90	0.290 ± 0.033	0.155 ± 0.008	16.9 ± 0.4	7.16 ± 0.25	0.081 ± 0.005
NF-32B	−1.11	0.186 ± 0.023	0.188 ± 0.008	19.8 ± 0.5	10.9 ± 0.5	0.106 ± 0.006
NF-29B	− 1.25	0.082 ± 0.021	0.075 ± 0.007	9.04 ± 0.28	6.47 ± 0.23	0.074 ± 0.005
NF-25B	− 1.42	0.074 ± 0.020	0.093 ± 0.006	11.4 ± 0.4	9.46 ± 0.37	0.072 ± 0.005
NF-24B	−1.50	0.143 ± 0.021	0.159 ± 0.007	5.25 ± 0.18	6.41 ± 0.24	0.077 ± 0.006
NF-23B	− 1.56	0.083 ± 0.026	0.085 ± 0.007	4.23 ± 0.18	4.34 ± 0.21	0.098 ± 0.007
NF-21B	− 1.63	0.057 ± 0.024	0.032 ± 0.007	1.91 ± 0.11	1.84 ± 0.10	0.048 ± 0.005
NF-17B	− 1.82	0.091 ± 0.020	0.064 ± 0.008	3.54 ± 0.15	2.35 ± 0.18	0.055 ± 0.005
NF-12B	−2.01	0.126 ± 0.022	0.118 ± 0.006	4.61 ± 0.15	3.67 ± 0.14	0.045 ± 0.005
NF-11B	−2.08	0.090 ± 0.019	0.093 ± 0.007	3.69 ± 0.13	3.43 ± 0.14	0.041 ± 0.006
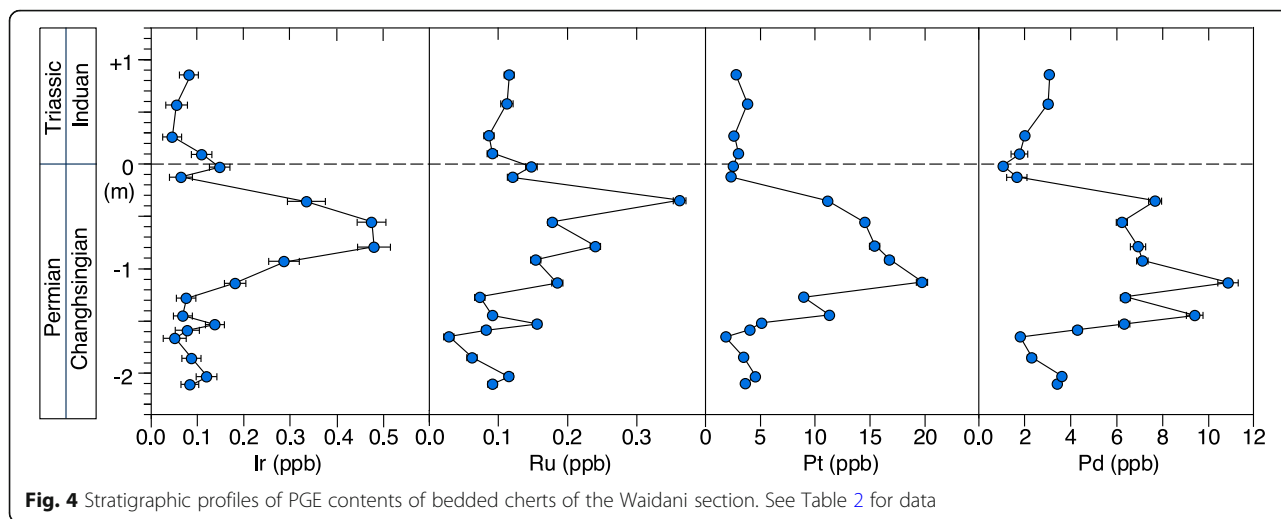
Fig. 4 Stratigraphic profiles of PGE contents of bedded cherts of the Waidani section. See Table 2 for data

There are two possibilities to explain this significant increase in $^3He_{ET}$ concentrations: (1) $^3He_{ET}$ concentrations reflect an approximately fourfold decrease in sedimentation rates or (2) the change reflects a significant increase in $^3He_{ET}$ influx. These possibilities were examined by establishing the floating astronomical timescale of the Upper Permian bedded chert, based on astronomical tuning. The whole-section power spectrum exhibits a dominant peak at 6.0 cm above the 99% confidence level (Fig. 6a). Assuming an average sedimentation rate for Changhsingian bedded chert of ~ 0.3 cm kyr^{-1}, 6.0 cm cycles may represent ~ 20 kyr precession cycles at the PTB. This is consistent with previous studies that demonstrated rhythmic alternations of chert and claystone beds over precession cycles of ~ 20 kyr (Ikeda and Tada 2014). A 20 kyr tuned astrochronology, anchored

Fig. 5 Bivariate plot of extraterrestrial ^3He ($^3He_{ET}$) versus excess Ir in samples from the Waidani section. Dashed line represents linear regression between the two. See Table 1 for $^3He_{ET}$ and Table 2 for excess Ir data

at the MEE horizon (251.942 Ma, Burgess et al. 2014), allows us to constrain the sedimentation rate for each bed of the Permian section. Results indicate that sedimentation rates varied from 0.2 to 0.5 cm kyr^{-1} (Fig. 6b), with no significant decrease for bedded chert in the topmost ~ 1.5 m of the Permian deposits. Therefore, we conclude that variations of ^3He in the Permian section record changes in the extraterrestrial ^3He flux with time rather than sedimentation rate. Spectral analysis of the precession-tuned time-series also reveals that the interval characterized by elevated $^3He_{ET}$ has a duration of ~ 500 kyr, with such a duration precluding large-impact and meteorite debris origins.

The extraterrestrial ^3He flux was calculated by multiplying the $^3He_{ET}$ concentration by the sedimentary mass accumulation rate (MAR, g cm^{-2} kyr^{-1}):

$$\text{Flux}^3He_{ET} = \left(\left[^3He_{ET}\right] \times \text{MAR}\right)/R \qquad (3)$$

where R is the fractional retention of ^3He after deposition on the sea floor (Farley 1995), ranging from 1 (total retention) to 0 (total loss). Using an approximate density for shale of 2.6 g cm^{-3}, we estimate an MAR value for the Permian section of 0.81 ± 0.18 g cm^{-2} kyr^{-1} (Table 1). Ignoring possible diffusive loss (R = 1), we estimate a maximum $^3He_{ET}$ flux of 0.27 ± 0.06 pcc cm^{-2} kyr^{-1} (1 pcc = 10^{-12} mL STP) before the MEE (Fig. 7). For a scenario where the MAR remained stable after the MEE, the $^3He_{ET}$ flux is tentatively estimated as 0.04–0.06 pcc cm^{-2} kyr^{-1} in the Triassic section. These values are consistent with those reported for Cenozoic and Cretaceous units (Farley et al. 1998, 2012).

We propose two possible mechanisms to explain the unique IDP signal recorded in the latest Permian samples: a cometary shower or collisions in the asteroid belt. Interplanetary dust particles are generally regarded as having
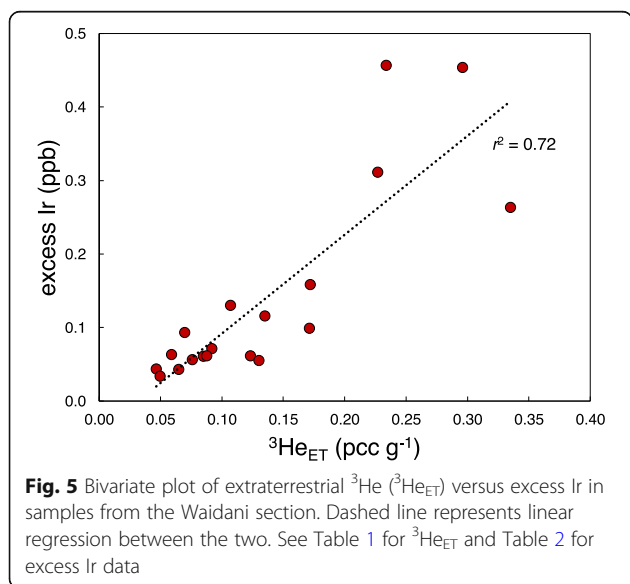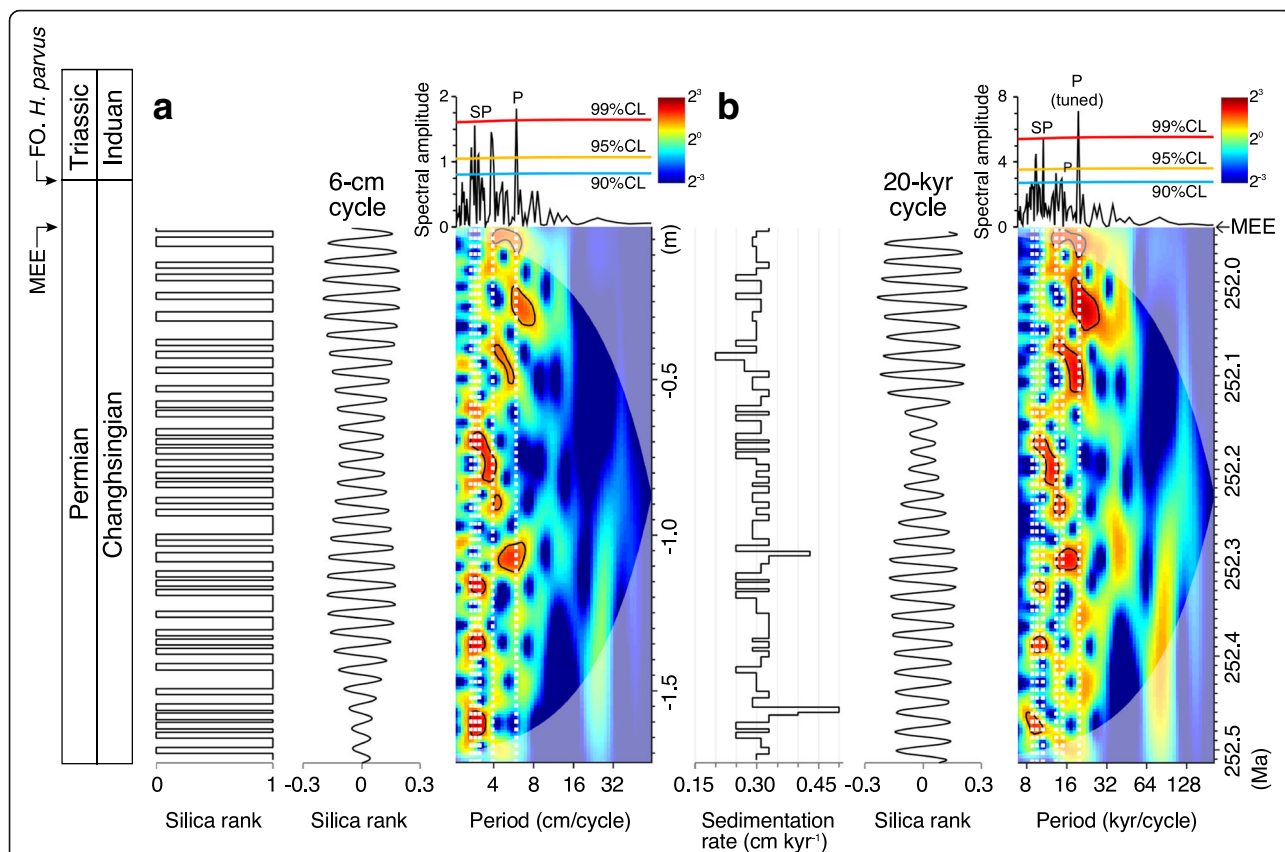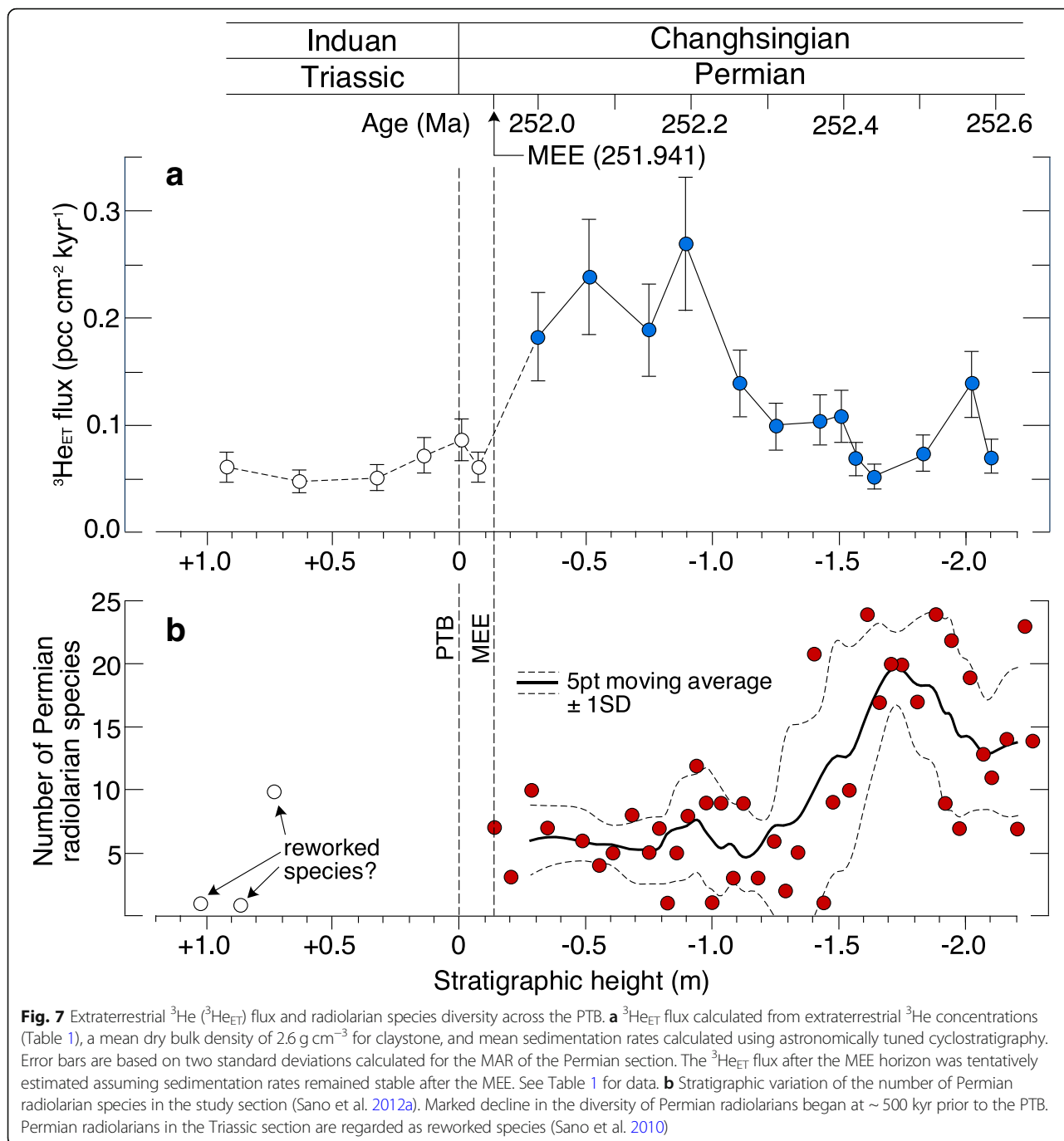
Fig. 6 Cyclostratigraphy and floating astronomical time scale (ATS) of the Waidani section. **a** Silica rank and frequency–amplitude modulations of the Upper Permian (Changhsingian) bedded chert sequence. The average sedimentation rate for the Changhsingian bedded chert is ~ 0.3 cm kyr^{-1}, so the extracted 6 cm cycle was converted to a long precession cycle (~ 20 kyr) for orbital tuning (Yao et al. 2015). **b** Variations in sedimentation rate for each bed, calculated from the Changhsingian ATS and frequency–amplitude modulations of orbital-tuned silica rank. Red, orange, and blue lines in the REDFIT spectra delineate 99%, 95%, and 90% confidence levels (CL) against red-noise background from a first-order autoregressive process, respectively (Schulz and Mudelsee 2002). P and SP at the spectral peaks represent precession and semi-precession (Berger et al. 2006; Soda et al. 2015), respectively. Black contours and shaded regions in the wavelet spectra indicate 95% CL against the red noise and cone of influence due to zero padding, respectively (Torrence and Compo 1998)

originated from dust-producing objects such as comets and asteroids (Kortenkamp and Dermott 1998). The particles migrate toward the Sun, driven by Poynting–Robertson and solar wind drag, and are continuously deposited on Earth. The Poynting–Robertson lifetime for micrometer-sized IDPs is of the order of 10^4–10^5 years (Burns et al. 1979), so most decay products from comets and asteroids are rapidly lost from the solar system. Cometary showers or collisions in the asteroid belt (Farley et al. 1998, 2006) result in episodes of elevated IDP flux to Earth over a few million years or less. Our estimate of the duration of peak ^{3}He$_{ET}$ flux immediately before the PTB is similar in magnitude to those of two well-documented Cenozoic ^{3}He$_{ET}$ events: a major asteroid collision in the late Miocene (Farley et al. 2006) and a dust shower generated from comets or asteroids in the late Eocene (Farley et al. 1998). These events were associated with longer periods (~ 1.5 Myr) of ^{3}He$_{ET}$ flux decay than is observed across the PTB (Farley et al. 2006, 2012). However, the

observed short duration of enhanced ^{3}He$_{ET}$ flux (~ 500 kyr) is consistent with the dynamic lifetime (10^4–10^5 years) of fine-grained dust liberated by a single asteroid disruption event. The timing of collision of the Erigone family of asteroids in the inner main asteroid belt is constrained to 220^{+60}_{-80} Ma, close to the PTB (Spoto et al. 2015). Our data are presently insufficient to identify an individual asteroid shower episode.

The present study indicates that an enhanced IDP flux event occurred simultaneously with a marked decline in the diversity of Permian radiolarians from ~ 500 kyr prior to the PTB (Fig. 7). A similar substantial pre-MEE decline of radiolarians has been reported in the Upper Permian (late Changhsingian) in South China (Feng et al. 2007; Feng and Algeo 2014). Furthermore, a recent statistical analysis of Permian ammonoids revealed that high turnover rates and extinction pulses occurred during the last ~ 700 kyr of the Permian (Kiessling et al. 2018). As a first approximation, it seems reasonable to assume that the

Fig. 7 Extraterrestrial ^{3}He (^{3}He$_{ET}$) flux and radiolarian species diversity across the PTB. **a** ^{3}He$_{ET}$ flux calculated from extraterrestrial ^{3}He concentrations (Table 1), a mean dry bulk density of 2.6 g cm^{-3} for claystone, and mean sedimentation rates calculated using astronomically tuned cyclostratigraphy. Error bars are based on two standard deviations calculated for the MAR of the Permian section. The ^{3}He$_{ET}$ flux after the MEE horizon was tentatively estimated assuming sedimentation rates remained stable after the MEE. See Table 1 for data. **b** Stratigraphic variation of the number of Permian radiolarian species in the study section (Sano et al. 2012a). Marked decline in the diversity of Permian radiolarians began at ~ 500 kyr prior to the PTB. Permian radiolarians in the Triassic section are regarded as reworked species (Sano et al. 2010)

pre-MEE declines of latest Permian radiolarians and ammonoids were related to an extraterrestrial event indicated by the ^{3}He record in the deep-sea PTB section of Japan.

Accretion and ablation of IDPs in Earth's ionosphere may affect the chemistry and aerosol distribution of the upper atmosphere (Grebowsky et al. 2002), providing a possible link between IDP accretion rate and global climate change (Muller and MacDonald 1997; Patterson and Farley 1998). The present study provides the first clear evidence of an extraterrestrial influence immediately prior to the PTB, and

a re-evaluation of the cause of the pre-MEE decline is required to confirm the link between extraterrestrial material flux and extinction-related global climate change.

Conclusions

Extraterrestrial ^{3}He is preserved in deep-sea bedded chert from a continuous PTB section at Waidani, Japan, which was deposited in the Panthalassa superocean. High ^{3}He/^{4}He ratios of up to 150 Ra were determined for acid-insoluble residues from the uppermost Permian

deposits, indicating the occurrence of extraterrestrial He hosted mainly in IDPs. The extraterrestrial ^{3}He fraction varies across the PTB with ^{3}He$_{ET}$ concentrations being higher in the topmost ~ 1.5 m of the studied Permian deposits (4–5 times higher than in the overlying Triassic unit). The ^{3}He$_{ET}$ flux to Earth across the PTB was estimated from the ^{3}He$_{ET}$ concentration and sedimentary mass accumulation rate of the Waidani PTB section, with the flux increasing over the last 500 kyr of the Permian. This unusual signal suggests a significant increase in the influx of IDPs, likely related to an asteroid shower in the inner solar system. High-resolution stratigraphy indicates that peak IDP flux occurred during the final 500 kyr of the Permian, concurrent with a pre-MEE decline in radiolarian diversity.

Additional files

Additional file 1: Figure S1. Map showing the location of the study area in central Japan. The deep-sea PTB section discovered in a radiolarian chert succession within the Mino Belt (Sano et al. 2012a) represents a Jurassic subduction-generated accretionary complex. (PDF 228 kb)

Additional file 2: Figure S2. Geological map of the Mt. Funabuseyama area. Map showing the location of the Waidani section (35°41′11″N, 136°40′27″E). (PDF 2034 kb)

Additional file 3: Figure S3. Mo and U enrichment factors and their ratios (Mo$_{EF}$/U$_{EF}$) for the studied section. Mo/U ratios are typically moderate (~ 3, similar to modern seawater) under weakly anoxic conditions and high (~ 9, three times that of modern seawater) under highly anoxic–euxinic bottom-water conditions (Takahashi et al. 2014; Algeo and Tribovillard 2009). See Additional file 2: Table S2 for data. (PDF 222 kb)

Additional file 4: Figure S4. Correlation coefficients for pairs of the elements/Al ratios determined in this study. Concentrations of the elements were normalized using Al concentrations to compensate the effect of biogenic SiO$_2$-dilution. Correlation coefficients (r) > 0.75 are indicated by colors according to the ranges of values. ∑REE represents total REE concentrations. (PDF 56 kb)

Additional file 5: Table S1. Major element compositions of claystone samples from the Waidani section. (XLSX 13 kb)

Additional file 6: Table S2. Trace element and REE compositions of claystone samples from the Waidani section. (XLSX 15 kb)

Abbreviations
CAI: Conodont alteration index; IDP: Interplanetary dust particle; MEE: Mass extinction event; PGE: Platinum group element; PTB: Permian–Triassic boundary

Authors' contributions
TO, NT, YS, and YI designed the study. TO, NT, MM, and YS performed the helium isotopic analyses. HS and AI performed the PGE analyses. TO performed the XRF analyses. KS performed the spectral analysis. All authors participated in the discussions to interpret the analytical results and aided in the writing of the manuscript. All authors read and approved the final manuscript.

Competing interests
The authors declare that they have no competing interests.

Publisher's Note
Springer Nature remains neutral with regard to jurisdictional claims in published maps and institutional affiliations.

Author details
[1]Department of Earth and Environmental Sciences, Kumamoto University, Kumamoto 860-8555, Japan. [2]Atmosphere and Ocean Research Institute, The University of Tokyo, Chiba 277-8564, Japan. [3]Ocean Resources Research Center for Next Generation, Chiba Institute of Technology, Chiba 275-0016, Japan. [4]Department of Earth and Planetary Sciences, Tokyo Institute of Technology, Tokyo 152-8550, Japan. [5]Department of Earth Science and Astronomy, The University of Tokyo, Tokyo 153-8902, Japan.

References
Agematsu S, Sano H, Sashida K (2014) Natural assemblages of Hindeodus conodonts from a Permian-Triassic boundary sequence, Japan. Palaeontology 57:1277–1289. https://doi.org/10.1111/pala.12114.

Algeo TJ, Kuwahara K, Sano H, Bates S, Lyons T, Elswick E, Hinnov L, Ellwood B, Moser J, Maynard JB (2011) Spatial variation in sediment fluxes, redox conditions, and productivity in the Permian-Triassic Panthalassic Ocean. Palaeogeogr Palaeoclimatol Palaeoecol 308:65–83. https://doi.org/10.1016/j.palaeo.2010.07.007.

Algeo TJ, Tribovillard N (2009) Environmental analysis of paleoceanographic systems based on molybdenum–uranium covariation. Chem Geol 268:211–225. https://doi.org/10.1016/j.chemgeo.2009.09.001.

Amari S, Ozima M (1985) Search for the origin of exotic helium in deep-sea sediments. Nature 317:520–522. https://doi.org/10.1038/317520a0.

Basu AR, Petaev MI, Poreda RJ, Jacobsen SB, Becker L (2003) Chondritic meteorite fragments associated with the Permian-Triassic boundary in Antarctica. Science 302:1388–1392. https://doi.org/10.1126/science.1090852.

Becker L, Poreda RJ, Basu AR, Pope KO, Harrison TM, Nicholson C, Iasky R (2004) Bedout: a possible end-Permian impact crater offshore of northwestern Australia. Science 304:1469–1476. https://doi.org/10.1126/science.1093925..

Becker L, Poreda RJ, Hunt AG, Bunch TE, Rampino M (2001) Impact event at the Permian-Triassic boundary: evidence from extraterrestrial noble gases in fullerenes. Science 291:1530–1533. https://doi.org/10.1126/science.1057243..

Berger A, Loutre MF, Mélice JL (2006) Equatorial insolation: from precession harmonics to eccentricity frequencies. Clim Past 2:131–136. https://doi.org/10.5194/cp-2-131-2006.

Burgess SD, Bowring S, Shen SZ (2014) High-precision timeline for Earth's most severe extinction. Proc Natl Acad Sci U S A 111:3316–3321. https://doi.org/10.1073/pnas.1317692111.

Burgess SD, Muirhead JD, Bowring SA (2017) Initial pulse of Siberian Traps sills as the trigger of the end-Permian mass extinction. Nat Commun 8:164. https://doi.org/10.1038/s41467-017-00083-9.

Burns JA, Lamy PL, Soter S (1979) Radiation forces on small particles in the solar system. Icarus 40:1–48. https://doi.org/10.1016/0019-1035(79)90050-2..

Colodner DC, Boyle EA, Edmond JM, Thomson J (1992) Post-depositional mobility of platinum, iridium and rhenium in marine sediments. Nature 358:402–404. https://doi.org/10.1038/358402a0.

Erwin DH (1994) The Permo-Triassic extinction. Nature 367:231–236. https://doi.org/10.1038/367231a0.

Evans NJ, Gregoire DC, Grieve RAF, Goodfellow WD, Veizer J (1993) Use of platinum-group elements for impactor identification: terrestrial impact craters and Cretaceous-Tertiary boundary. Geochim Cosmochim Acta 57:3737–3748. https://doi.org/10.1016/0016-7037(93)90152-M.

Farley KA (1995) Cenozoic variations in the flux of interplanetary dust recorded by ^{3}He in a deep-sea sediment. Nature 376:153–156. https://doi.org/10.1038/376153a0.

Farley KA, Montanari A, Coccioni R (2012) A record of the extraterrestrial ^{3}He flux through the Late Cretaceous. Geochim Cosmochim Acta 84:314–328. https://doi.org/10.1016/j.gca.2012.01.015.

Farley KA, Montanari A, Shoemaker EM, Shoemaker CS (1998) Geochemical evidence for a comet shower in the Late Eocene. Science 280:1250–1253. https://doi.org/10.1126/science.280.5367.1250..

Farley KA, Mukhopadhyay S (2001) An extraterrestrial impact at the Permian-Triassic boundary? Science 293:2343. https://doi.org/10.1126/science.293.5539.2343a.

Farley KA, Vokrouhlicky D, Bottke WF, Nesvorny D (2006) A late Miocene dust shower from the break-up of an asteroid in the main belt. Nature 439:295–297. https://doi.org/10.1038/nature04391.

Farley KA, Ward P, Garrison G, Mukhopadhyay S (2005) Absence of extraterrestrial ^{3}He in Permian-Triassic age sedimentary rocks. Earth Planet Sci Lett 240:265–275. https://doi.org/10.1016/j.epsl.2005.09.054.

Feng Q, He W, Gu S, Meng Y, Jin Y, Zhang F (2007) Radiolarian evolution during the latest Permian in South China. Glob Planet Chang 55:177–192. https://doi.org/10.1016/j.gloplacha.2006.06.012.

Feng QL, Algeo TJ (2014) Evolution of oceanic redox conditions during the Permo-Triassic transition: evidence from deepwater radiolarian facies. Earth-Sci Rev 137:34–51. https://doi.org/10.1016/j.earscirev.2013.12.003.

Genge MJ, Engrand C, Gounelle M, Taylor S (2008) The classification of micrometeorites. Meteorit Planet Sci 43:497–515. https://doi.org/10.1111/j.1945-5100.2008.tb00668.x.

Grebowsky JM, Moses JI, Pesnell WD (2002) Meteoric material—an important component of planetary atmospheres. In: Mendillo M, Nagy A, Waite JH (eds) Atmospheres in the solar system: comparative aeronomy. Geophysical monograph series, vol 130 American Geophysical Union, 235–244. doi: https://doi.org/10.1029/130GM15.

Heck PR, Schmitz B, Baur H, Wieler R (2008) Noble gases in fossil micrometeorites and meteorites from 470 Myr old sediments from southern Sweden, and new evidence for the L-chondrite parent body breakup event. Meteorit Planet Sci 43:517–528. https://doi.org/10.1111/j.1945-5100.2008.tb00669.x.

Ikeda M, Tada R (2014) A 70 million year astronomical time scale for the deep-sea bedded chert sequence (Inuyama, Japan): implications for Triassic–Jurassic geochronology. Earth Planet Sci Lett 399:30–43. https://doi.org/10.1016/j.epsl.2014.04.031.

Ishikawa A, Senda R, Suzuki K, Dale CW, Meisel T (2014) Re-evaluating digestion methods for highly siderophile element and ^{187}Os isotope analysis: evidence from geological reference materials. Chem Geol 384:27–46. https://doi.org/10.1016/j.chemgeo.2014.06.013.

Isozaki Y (1997) Permo-Triassic boundary superanoxia and stratified superocean: records from lost deep-sea. Science 276:235–238. https://doi.org/10.1126/science.276.5310.235.

Kiessling W, Schobben M, Ghaderi A, Hairapetian V, Leda L, Korn D (2018) Pre–mass extinction decline of latest Permian ammonoids. Geology 46:283–286. https://doi.org/10.1130/G39866.1.

Koeberl C, Farley KA, Peucker-Ehrenbrink B, Sephton MA (2004) Geochemistry of the end-Permian extinction event in Austria and Italy: no evidence for an extraterrestrial component. Geology 32:1053–1056. https://doi.org/10.1130/G20907.1.

Kortenkamp SJ, Dermott SF (1998) Accretion of interplanetary dust particles by the Earth. Icarus 135:469–495. https://doi.org/10.1006/icar.1998.5994.

Laskar J, Robutel P, Joutel F, Gastineau M, Correia ACM, Levrard B (2004) A long-term numerical solution for the insolation quantities of the Earth. Astron Astrophys 428:261–285. https://doi.org/10.1051/0004-6361:20041335.

Marcantonio F, Kumar N, Stute M, Anderson RF, Seidl MA, Schlosser P, Mix A (1995) A comparative study of accumulation rates derived by He and Th isotope analysis of marine sediments. Earth Planet Sci Lett 133:549–555. https://doi.org/10.1016/0012-821X(95)00079-R.

Matsuda T, Isozaki Y (1991) Well-documented travel history of Mesozoic pelagic chert in Japan: from remote ocean to subduction zone. Tectonics 10:475–499. https://doi.org/10.1029/90TC02134.

McGee D, Mukhopadhyay S (2013) Extraterrestrial He in sediments: from recorder of asteroid collisions to timekeeper of global environmental changes. In: Burnard P (ed) The noble gases as geochemical tracers. Springer, Berlin, pp 155–176. https://doi.org/10.1007/978-3-642-28836-4_7..

McLennan SM (2001) Relationships between the trace element composition of sedimentary rocks and upper continental crust. Geochem Geophys Geosyst 2:200GC000109. https://doi.org/10.1029/2000GC000109..

Mukhopadhyay S, Farley KA (2006) New insights into the carrier phase(s) of extraterrestrial ^{3}He in geologically old sediments. Geochim Cosmochim Acta 70:5061–5073. https://doi.org/10.1016/j.gca.2006.06.1566.

Muller RA, MacDonald GJ (1997) Glacial cycles and astronomical forcing. Science 277:215–218. https://doi.org/10.1126/science.277.5323.215..

Onoue T, Nakamura T, Haranosono T, Yasuda C (2011) Composition and accretion rate of fossil micrometeorites recovered in Middle Triassic deep-sea deposits. Geology 39:567–570. https://doi.org/10.1130/G31866.1.

Onoue T, Sato H, Nakamura T, Noguchi T, Hidaka Y, Shirai N, Ebihara M, Osawa T, Hatsukawa Y, Toh Y, Koizumi M, Harada H, Orchard MJ, Nedachi M (2012) Deep-sea record of impact apparently unrelated to mass extinction in the Late Triassic. Proc Natl Acad Sci U S A 109:19134–19139. https://doi.org/10.1073/pnas.1209486109.

Paillard D, Labeyrie L, Yiou P (1996) Macintosh program performs time-series analysis. EOS 77:379. https://doi.org/10.1029/96EO00259.

Patterson DB, Farley KA (1998) Extraterrestrial ^{3}He in seafloor sediments: evidence for correlated 100 kyr periodicity in the accretion rate of interplanetary dust, orbital parameters, and Quaternary climate. Geochim Cosmochim Acta 62:3669–3682. https://doi.org/10.1016/S0016-7037(98)00263-4.

Patterson DB, Farley KA, Schmitz B (1998) Preservation of extraterrestrial ^{3}He in 480-Ma-old marine limestones. Earth Planet Sci Lett 163:315–325. https://doi.org/10.1016/S0012-821X(98)00197-6.

Ramezani J, Bowring SA (2017) Advances in numerical calibration of the Permian timescale based on radioisotopic geochronology. Geol Soc London Spec Publ 450(1):51–60. https://doi.org/10.1144/SP450.17.

Sano H, Kuwahara K, Yao A, Agematsu S (2010) Panthalassan seamount-associated Permian-Triassic boundary siliceous rocks, Mino terrane, Central Japan. Paleont Res 14:293–314. https://doi.org/10.2517/1342-8144-14.4.293.

Sano H, Kuwahara K, Yao A, Agematsu S (2012b) Stratigraphy and age of the Permian-Triassic boundary siliceous rocks of the Mino terrane in the Mt. Funabuseyama area, Central Japan. Paleont Res 16:124–145. https://doi.org/10.2517/1342-8144-16.2.124.

Sano H, Wada T, Naraoka H (2012a) Late Permian to Early Triassic environmental changes in the Panthalassic Ocean: record from the seamount-associated deep-marine siliceous rocks, Central Japan. Palaeogeogr Palaeoclimatol Palaeoecol 363:1–10. https://doi.org/10.1016/j.palaeo.2012.07.018.

Sano Y (2017) Helium Isotopes. In: White WM (ed) Encyclopedia of geochemistry: a comprehensive reference source on the chemistry of the Earth. Encyclopedia of Earth Sciences Series doi:https://doi.org/10.1007/978-3-319-39193-9_205-1.

Sano Y, Marty B, Burnard P (2013) Noble gases in the atmosphere. In: Burnard P (ed) The noble gases as geochemical tracers. Springer, Berlin, pp 17–31. https://doi.org/10.1007/978-3-642-28836-4_2..

Schulz M, Mudelsee M (2002) REDFIT: estimating red-noise spectra directly from unevenly spaced paleoclimatic time series. Comput Geosci 28:421–426. https://doi.org/10.1016/S0098-3004(01)00044-9.

Soda K, Onoue T, Ikeda M (2015) Cyclostratigraphic examination of Middle Triassic (Anisian) bedded chert in the Chichibu Belt from Tsukumi area, eastern Kyushu, Japan. J Geol Soc Jpn 121:147–152. https://doi.org/10.5575/geosoc.2015.0008.

Spoto F, Milani A, Knezevic Z (2015) Asteroid family ages. Icarus 257:275–289. https://doi.org/10.1016/j.icarus.2015.04.041.

Takahashi S, Yamasaki S, Ogawa Y, Kimura K, Kaiho K, Yoshida T, Tsuchiya N (2014) Bioessential element-depleted ocean following the euxinic maximum of the end-Permian mass extinction. Earth Planet Sci Lett 393:94–104. https://doi.org/10.1016/j.epsl.2014.02.041.

Torrence C, Compo GP (1998) A practical guide to wavelet analysis. Bull Am Meteor Soc 79:61–78. https://doi.org/10.1175/1520-0477(1998)079<0061:APGTWA>2.0.CO;2.

Uno K, Onoue T, Hamada K, Hamami S (2012) Palaeomagnetism of Middle Triassic red bedded cherts from southwest Japan: equatorial palaeolatitude of primary magnetization and widespread secondary magnetization. Geophys J Int 189:1383–1398. https://doi.org/10.1111/j.1365-246X.2012.05462.x.

Wignall PB (2007) The End-Permian mass extinction - how bad did it get? Geobiology 5:303–309. https://doi.org/10.1111/j.1472-4669.2007.00130.x.

Winckler G, Fischer H (2006) 30,000 years of cosmic dust in Antarctic ice. Science 313:491. https://doi.org/10.1126/science.1127469..

Yao X, Zhou Y, Hinnov LA (2015) Astronomical forcing of a Middle Permian chert sequence in Chaohu, South China. Earth Planet Sci Lett 422:206–221. https://doi.org/10.1016/j.epsl.2015.04.017.